J Adv Ceram

Research Article

Structural evolution-driven enhancement of thermoelectric performance in Bi–S–Se solid solutions

Kun Huang, Zi-Yuan Wang, Chong-Yu Wang, Yi-Xin Zhang, Ye-Hua Jiang, Jing Feng✉, Zhen-Hua Ge✉

Cite this article: Huang K, Wang Z-Y, Wang C-Y, et al. *J Adv Ceram* 2026, **15**(2): 9221239. https://doi.org/10.26599/JAC.2026.9221239

ABSTRACT: Bismuth sulfide (Bi_2S_3) has garnered extensive attention for thermoelectric (TE) applications due to its earth abundance, nontoxicity, and ultralow lattice thermal conductivity. However, simultaneously improving its electrical and thermal properties remains challenging due to the strong coupling between these parameters. Herein, we propose a structural evolution strategy to synergistically optimize the electrical and thermal transport properties of Bi_2S_3-based TE compounds. By leveraging the distinct crystal structures of Bi_2S_3 and Bi_2Se_3, alloying Se at S sites successfully reconstructs the carrier transport channels within the Bi_2S_3 matrix, thereby facilitating carrier mobility. Additionally, the weakened chemical bonding leads to a significant increase in carrier concentration, approaching the optimal range. Furthermore, the structural evolution from particle-like to lamellar grains, coupled with the large mass difference between Se and S, induces lattice distortion that effectively reduces the lattice thermal conductivity. Combining the dramatically enhanced power factor and ultralow thermal conductivity, an optimized figure of merit (ZT) of 0.38 at 623 K is achieved in the Bi_2SSe_2 solid solution. This structural evolution strategy offers a promising avenue for enhancing the TE performance of binary compounds.

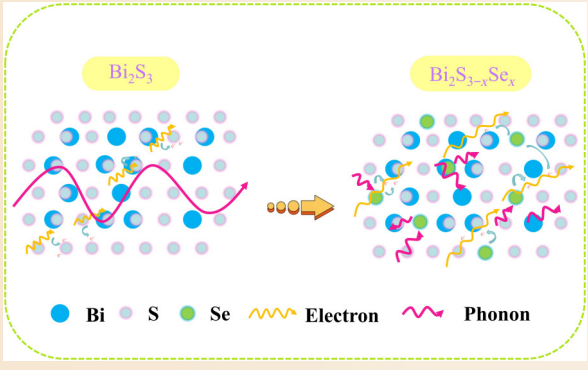

KEYWORDS: functional ceramics; thermoelectric material; Bi_2S_3; structural evolution

1 Introduction

Thermoelectric [1–9] (TE) technology, which enables the direct conversion of thermal energy into electrical energy, presents a promising solution for the capture and utilization of mid-range waste heat (i.e., heat within a moderate temperature range). This technology holds significant potential for advancing sustainable energy systems. The efficiency of TE materials is often quantified by the dimensionless figure of merit ($ZT = \sigma S^2 T/\kappa$) [10,11] and the power factor (PF = σS^2), where S, σ, κ, and T represent the Seebeck coefficient, electrical conductivity, thermal conductivity, and temperature, respectively. To improve TE performance, research efforts typically focus on reducing thermal conductivity or enhancing the electrical properties of the material. However, the strong interdependence among electrical conductivity, Seebeck coefficient, and thermal conductivity often hinders overall performance improvements. Since the beginning of research on TE materials, considerable attention has been devoted to improving TE performance by increasing the power factor and reducing thermal conductivity. In recent decades, a variety of novel TE material systems have emerged, such as PbTe [12–14], PbSe [15–17], Cu_3SbSe_4 [18,19], and Mg_3Sb_2 [20–22]. These improvements have been achieved through strategies including lattice dislocations [23], lattice planification [24], Ostwald ripening [25], unconventional doping [18], band degeneration [26], and other advanced techniques [27–30] to optimize TE properties. These new systems have remarkably contributed to improving the ZT of TE materials. However, they still present notable challenges. Pb, being a toxic element, poses difficulties for safe commercialization. Additionally, the Cu in Cu_3SbSe_4 materials complicates the use of inexpensive copper sheets in TE devices, as Cu migration can damage the copper plate. The recently popular Mg_3Sb_2 material is prone to oxidation during the synthesis process, and the highly reactive nature of the Mg element in this process increases the risk of safety accidents, presenting an enormous challenge for commercial production. As a traditional TE material, Bi_2S_3 [31–33] possesses several advantages, including the high abundance of sulfur, low cost, nontoxicity, ease of synthesis, and stable TE performance. To overcome these limitations, significant efforts have been focused on optimizing the transport properties of Bi_2S_3. Common strategies include carrier concentration optimization via donor doping [34,35] and lattice thermal conductivity reduction through nanostructuring [36,37]. Although these approaches have improved the ZT values to some extent, achieving a simultaneous enhancement in power factor and reduction in thermal conductivity remains challenging due to

Faculty of Materials Science and Engineering, Kunming University of Science and Technology, Kunming 650093, China.

✉ Corresponding authors. E-mail: J. Feng, jingfeng@kust.edu.cn; Z. Ge, zge@kust.edu.cn

Received: October 28, 2025; Revised: December 12, 2025; Accepted: January 3, 2026

the strong coupling of thermoelectric parameters. Motivated by these challenges, we propose a "structural evolution" strategy rather than simple doping. Unlike conventional impurity doping, forming a solid solution with Se—which is isovalent to S—allows for continuous tuning of the crystal symmetry. In this study, a structural evolution strategy is employed by introducing Se into the Bi_2S_3 matrix through a solid solution, where Se atoms replace S atoms. This substitution reconstructs the carrier transport channels, leading to a synergistic enhancement of carrier concentration and mobility, attributed to the weaker electron-binding ability of Se than that of S. Additionally, the large atomic mass difference between Se and S induces lattice distortion, which enhances phonon scattering and reduces lattice thermal conductivity. This approach facilitates the development of Bi–S–Se TE materials with tunable electrical transport properties. As a result, all Se-substituted solid solutions exhibit higher *ZT* values than Bi_2S_3, with Bi_2SSe_2 achieving a maximum *ZT* of 0.38 at 623 K. This work establishes a general strategy for enhancing TE performance by leveraging structure evolution via solid solution.

2 Experimental details

2.1 Synthesis

High-purity Bi powder (4N), S powder (4N), and Se powder (4N) were used for the synthesis. All raw materials were purchased from Shanghai Aladdin Biochemical Technology Co., Ltd. (China).The powders were meticulously loaded into a quartz tube inside a glove box maintained under an argon environment. The quartz tubes were then hermetically sealed using a hydroxide flame sealing technique in a vertical furnace under high-vacuum conditions (pressure < 10^{-4} Pa). The sealed tubes were gradually heated over 24 h to reach a final temperature of 1173 K. This temperature was sustained for 12 h, followed by a controlled cooling phase that gradually lowered the temperature to 623 K within 6 h. Subsequently, annealing was conducted at this temperature for 12 h. In the final stage, the samples underwent cooling to room temperature in synchrony with the furnace's natural cooldown. The resulting ingots were crushed into powder using a mortar and then ground for 15 min in air. A bulk sample with dimensions of ϕ15 mm × 3 mm was fabricated by plasma sintering the milled powder using a spark plasma sintering machine (SPS; Sumitomo SPS6321x, Japan) for 5 min in a graphite mold under an axial pressure of 40 MPa and a temperature of 623 K. Two samples were extracted from the bulk material for the measurement of electrical conductivity, Seebeck coefficient, and thermal diffusivity. Furthermore, energy-dispersive X-ray spectroscopy (EDS) equipped on a scanning electron microscope (FESEM, Sigma 300, Zeiss, Germany) was used to determine the actual chemical compositions of the samples, and the relevant description has been included in Table S1 in the Electronic Supplementary Material (ESM).

2.2 Phase structure and microstructure characterizations

The phase structure was analyzed using an X-ray diffractometer (XRD; Miniflex600, Rigaku, Japan) using Cu Kα (λ = 1.5406 Å) radiation, with continuous scanning at a rate of 5 (°)/min over a 2θ range of 20°–70°. The microscopic morphology was observed using a field emission scanning electron microscope (FESEM; Zeiss Sigma 300, Zeiss, Germany).

2.3 Thermoelectric transport properties

The Seebeck coefficient and electrical resistivity were concurrently measured over a temperature range of approximately 323–623 K using a commercial measurement system (ZEM-3, ULVAC-RIKO, Japan). The Hall coefficient was determined at room temperature with a Hall tester (HMS7000, ECOPIA, Republic of Korea). The thermal diffusion coefficient (*D*) was obtained via a laser flash method using a laser thermal conductivity meter (LFA_467, NETZSCH, Germany). Thermal conductivity was then calculated using the equation $\kappa = Dc_p\rho$, where *D* is the thermal diffusion coefficient; c_p represents the specific heat capacity; ρ is the bulk density of the sample, determined via Archimedes' method. The specific heat capacity was calculated using the equation $c_p = 3N_Ak_B$, where N_A is Avogadro's number and k_B is the Boltzmann constant. Furthermore, $Bi_2S_{0.5}Se_{2.5}$ exhibits high anisotropy compared to Bi_2Se_3 materials. The thermoelectric properties measured both perpendicular and parallel to the SPS pressure direction were supplemented in the ESM. Ultimately, the thermoelectric properties perpendicular to the SPS pressure direction demonstrate superior performance. Detailed results are provided in Figs. S4 and S5 in the ESM.

2.4 Mechanical properties

The mechanical properties, microhardness, and Young's modulus were measured using a nanoindenter (iMicro, KLA, USA).

2.5 Calculations

First-principles calculations were performed using the Vienna *Ab Initio* simulation package (VASP) based on density functional theory (DFT). The projector-augmented wave (PAW) method was employed to model the interactions between electrons and ions, while the Perdew–Burke–Ernzerhof (PBE) form of the generalized gradient approximation (GGA) was adopted as the exchange-correlation functional. A plane-wave cutoff energy of 450 eV was used, along with a Gaussian smearing width of 0.05 eV to reasonably describe orbital occupancies.

Brillouin zone sampling was carried out using a Monkhorst–Pack *k*-point mesh of 3×4×4, and convergence tests with higher k-point densities were conducted to ensure accuracy.

All crystal structure models were generated using a disorder code to explore all possible configurations, from which the lowest-energy structure was selected for full structural optimization. The band structures were computed based on high-symmetry points in the Brillouin zone, identified using VASPKIT for auxiliary analysis. Chemical bonding characteristics were analyzed through crystal orbital Hamilton population (COHP) calculations, as implemented in the LOBSTER package. More detailed calculations and experiments are provided in the ESM.

3 Results and discussion

To understand the synergistic optimization of electrical and thermal properties, the atomic-scale evolution mechanism upon Se incorporation was analyzed (Fig. 1). Bi_2S_3 exhibits significant potential for TE applications owing to its low lattice thermal conductivity and high Seebeck coefficient; however, its inherently low electrical conductivity limits its overall TE performance. To address this limitation, Se is incorporated into the Bi_2S_3 matrix via solid solution, where the substitution of S with the Group 16 element Se induces a structural evolution that enhances electronic transport while simultaneously reducing lattice thermal conductivity.

Figure 1(a) displays the intrinsic crystal structure of pure Bi_2S_3, where strong electron binding leads to a low carrier concentration, limiting electrical conductivity. Figure 1(b) illustrates the evolution of both electrical and thermal transport properties for $Bi_2S_{3-x}Se_x$

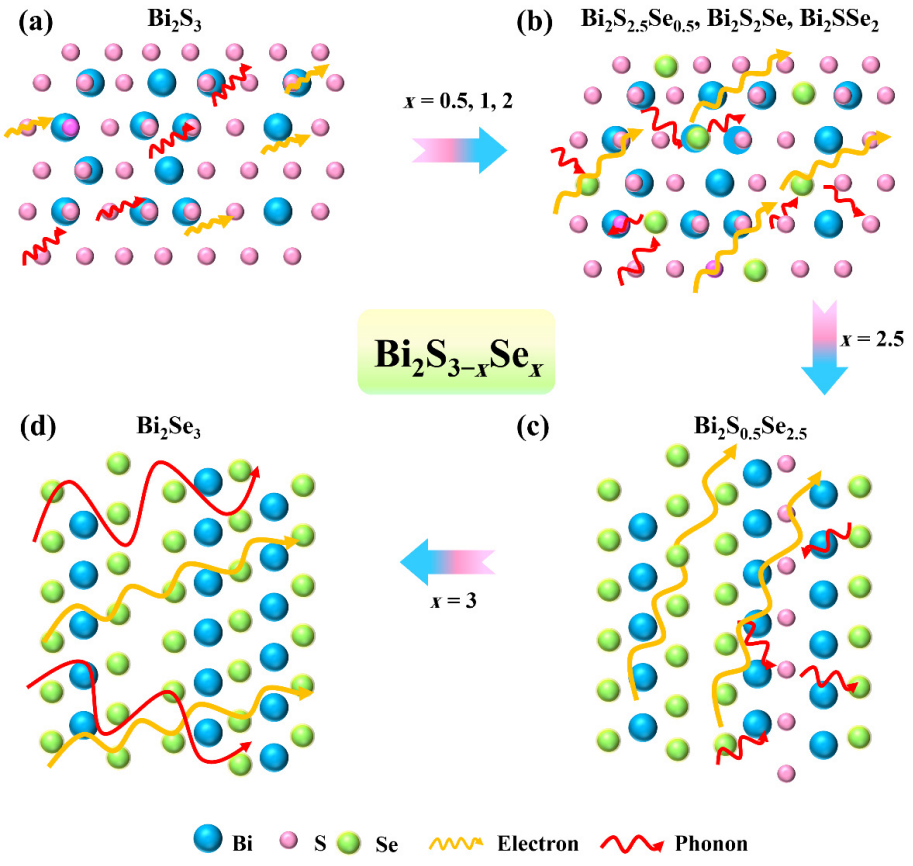

Fig. 1 Schematic illustration of mechanism governing electrical and thermal properties of Se-substituted Bi_2S_3 solid solution.

(x = 0.5, 1, and 2) as Se is gradually introduced. Owing to the lower electronegativity of Se than that of S, it acts as a negative center with a weaker electron-binding capability. This modification reconstructs the carrier transport channels and facilitates the excitation of additional charge carriers, which in turn increases both the carrier concentration and mobility. Furthermore, the mass difference between Se (atomic mass: 78.94) and S (atomic mass: 32.06) induces pronounced fluctuation scattering, intensifying point-defect scattering and reducing the lattice thermal conductivity.

Figure 1(c) presents the crystal structure evolution for the composition with x = 2.5, where a phase transition occurs from the Bi_2S_3 phase to the Bi_2Se_3 phase. This results in a layered structure that optimizes the carrier transport pathways. In this composition, the minor presence of S functions as a dilute solid solution within the Bi_2Se_3 matrix, potentially introducing localized electronic states that boost both carrier mobility and concentration. Additionally, certain chemical bonds in Bi_2S_3, $Bi_2S_{2.5}Se_{0.5}$, Bi_2SSe_2, and Bi_2S_2Se exhibit more antibonding characteristics, which contribute to the further reduction in lattice thermal conductivity, as corroborated by COHP analysis.

Figure 1(d) shows the crystal structure of pure Bi_2Se_3. In this structure, the complete replacement of S by Se eliminates the electronic transport barriers typically associated with S, leading to a marked improvement in carrier mobility. However, the intrinsically low carrier concentration in Bi_2Se_3 limits its electrical conductivity, which remains lower than that of $Bi_2S_{0.5}Se_{2.5}$. In addition, Bi_2Se_3 is completely unimpeded by phonon scattering in the direction perpendicular to the SPS pressure due to its special layered structure, resulting in a higher lattice thermal conductivity than the other samples.

Figure 2 illustrates that Se can be continuously incorporated

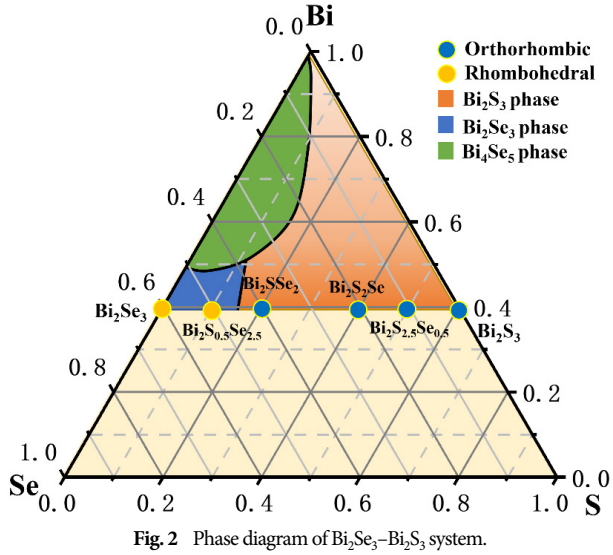

Fig. 2 Phase diagram of Bi_2Se_3–Bi_2S_3 system.

into the Bi_2S_3 system. Alloying by substituting Se for S induces a structural evolution that reconstructs the carrier transport channels, thereby enhancing carrier mobility and electrical transport performance. Structural analyses reveal that as the Se content increases, the material retains the Bi_2S_3 phase with an orthorhombic crystal structure when the Se content is ≤ 2.5, indicating that no phase transition occurs within this range. However, when the Se content exceeds 2.5, the crystal structure transforms into the Bi_2Se_3 phase, underscoring the profound impact of the solid solution process on the crystal structure.

The phase purity and crystal structure evolution of the synthesized samples were examined via XRD patterns (Fig. 3). As

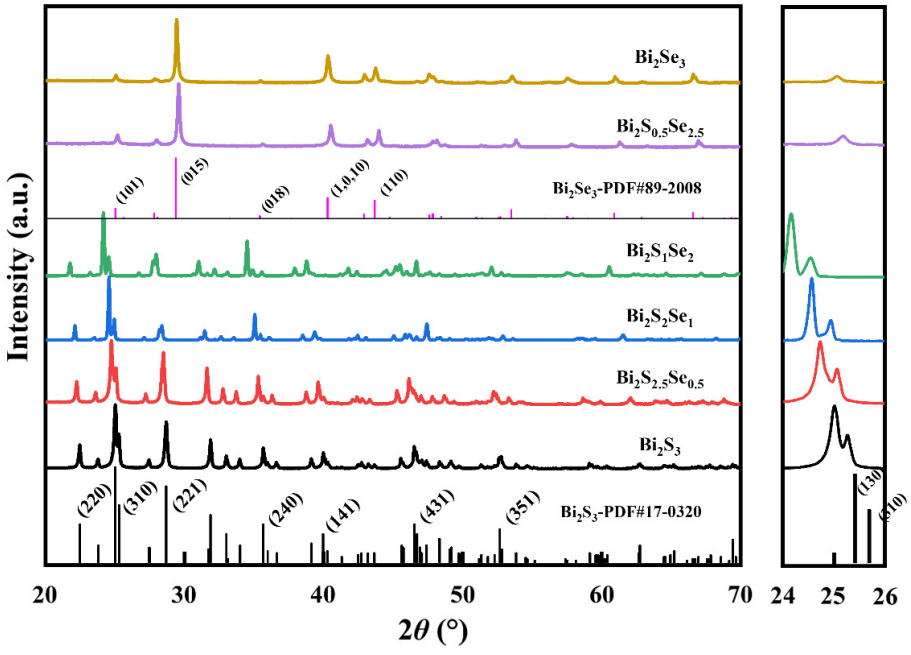

Fig. 3 XRD patterns of bulk samples: Bi_2S_3, $Bi_2S_{2.5}Se_{0.5}$, Bi_2S_2Se, Bi_2SSe_2, $Bi_2S_{0.5}Se_{2.5}$, and Bi_2Se_3.

the Se content increases, Bi_2S_3, $Bi_2S_{2.5}Se_{0.5}$, Bi_2SSe_2, and Bi_2S_2Se display an orthorhombic phase consistent with Bi_2S_3. Bi_2Se_3 and $Bi_2S_{2.5}Se_{0.5}$ show a monoclinic phase corresponding to Bi_2Se_3. These findings align with the phase diagram shown in Fig. 2. With increasing Se content, the diffraction peak gradually shifts toward lower angles, which is attributed to the substitution of S by Se, given the larger ionic radius of Se^{2-} (198 pm) than that of S^{2-} (184 pm).

To accurately characterize the structural evolution and confirm the formation of solid solutions beyond qualitative peak shifts, we performed quantitative Rietveld refinements on the XRD patterns of the $Bi_2S_{3-x}Se_x$ series. The refinement profiles (Fig. S6 in the ESM) show excellent agreement between the observed and calculated intensities. As detailed in Table 1, the extracted lattice parameters reveal a systematic lattice expansion driven by the substitution of larger Se atoms. Specifically, in the orthorhombic phase region (x = 0–2), the unit cell volume (V_{cell}) increases significantly from 501.29 Å^3 (Bi_2S_3) to 546.25 Å^3 (Bi_2SSe_2), accompanied by the continuous elongation of the a, b, and c axes. Similarly, the rhombohedral phase (x = 2.5–3) exhibits a volume expansion from 419.82 to 424.50 Å^3. This quantitative trend strictly follows Vegard's law within each phase regime, providing robust evidence for the successful synthesis of the Bi–S–Se system.

Table 1 Lattice parameters and unit cell volumes of $Bi_2S_{3-x}Se_x$ series

Sample	a	b	c	V_{Cell} (Å^3)
Bi_2S_3	11.19469	3.98248	11.14446	501.288
$Bi_2S_{2.5}Se_{0.5}$	11.39665	4.00143	11.20729	511.086
Bi_2S_2Se	11.48944	4.02178	11.27926	521.191
Bi_2SSe_2	11.68480	4.07645	11.46800	546.250
$Bi_2S_{0.5}Se_{2.5}$	4.12179	4.12179	28.53404	419.822
Bi_2Se_3	4.13705	4.13705	28.63982	424.504

Figure 4 presents the microstructures of a series of Bi_2S_3-based materials synthesized via Se solid solution, including Bi_2Se_3, various $Bi_2S_{3-x}Se_x$ compositions, and pristine Bi_2S_3. SEM images at the 300 nm scale reveal a marked transformation from particle-like to lamellar grains with higher Se content. This structural evolution effectively reconstructs the carrier transport channels,

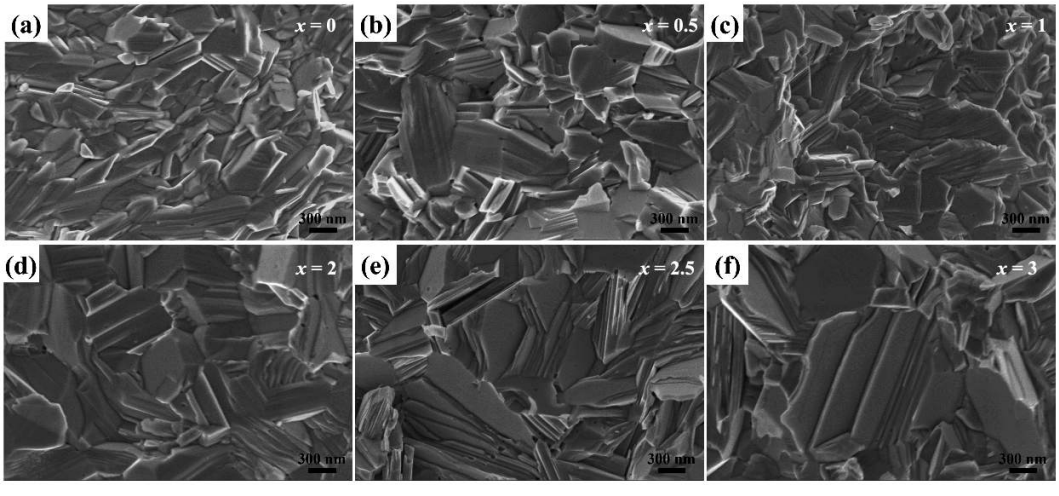

Fig. 4 SEM images of $Bi_2S_{3-x}Se_x$ (x = 0, 0.5, 1, 2, 2.5, and 3).

leading to a notable enhancement in carrier mobility. Subsequent measurements of carrier mobility and concentration further corroborate the observed improvement in TE performance.

The electrical transport properties of the Bi–S–Se system exhibit a strong dependence on the Se content (Fig. 5). Specifically, the electrical conductivity at room temperature rises monotonically with the addition of Se (Fig. 5(a)), increasing from 0.28 S·cm^{-1} for pristine Bi_2S_3 to 5.67 S·cm^{-1} for $Bi_2S_{2.5}Se_{0.5}$, 39.13 S·cm^{-1} for Bi_2S_2Se, 88.45 S·cm^{-1} for Bi_2SSe_2, and 102.91 S·cm^{-1} for Bi_2Se_3. Notably, $Bi_2S_{0.5}Se_{2.5}$ exhibits a significantly higher conductivity of 1656.54 S·cm^{-1}, which represents an increase of approximately three orders of magnitude compared to the room-temperature conductivity of Bi_2S_3. This substantial improvement is primarily attributed to the relatively high conductivity of Bi_2Se_3. $Bi_2S_{0.5}Se_{2.5}$ can be viewed as the introduction of a small amount of S in Bi_2Se_3. Both S and Se belong to the same group (Group 16) in the periodic table, yet the electronegativity of S is generally considered to be higher than that of Se. According to the Pauling electronegativity scale, S has an electronegativity of approximately 2.58, whereas Se has an electronegativity of approximately 2.55. Although the values are close, the slightly higher electronegativity of S suggests a stronger tendency to attract electrons than Se, which may account for the observed decrease in carrier concentration. Additionally, the introduction of S may lead to the formation of specific defect states, which enhance electron localization, thereby improving both carrier concentration and mobility, as confirmed by the experimental results shown in Fig. 5(b). The incorporation of Se in Bi_2S_3 enables the tuning of its electrical conductivity over three orders of magnitude. According to the equation $\sigma = ne\mu$, where n is the charge carrier concentration; e is the elementary charge; μ is the carrier mobility, this enhancement can be attributed to changes in the carrier density and mobility. This significant increase in conductivity is ascribed to the simultaneous enhancement of carrier concentration and mobility. While carrier concentration typically shares an inverse relationship with mobility, their simultaneous increase here is driven by specific electronic structure evolutions. First, the band structure analysis (Fig. 6) reveals that Se substitution increases the dispersion (curvature) of the conduction band minimum. This implies a reduction in the carrier effective mass (m^*), which is directly proportional to mobility ($\mu = e\tau/m^*$), where τ is the relaxation time. Second, the sharp increase in carrier concentration (reaching 10^{19} cm^{-3}) enhances the dielectric screening effect. The high density of free carriers effectively screens the long-range Coulomb potential of ionized impurities, thereby weakening ionized impurity scattering. These electronic mechanisms, combined with the phase transition to the layered Bi_2Se_3 structure that provides unimpeded transport channels, result in the observed surge in mobility. Figure 5(c) presents the temperature-dependent Seebeck coefficient (S). This trend aligns well with the Pisarenko relation, which states that the Seebeck coefficient is inversely proportional to the carrier concentration ($n^{2/3}$). As observed in Fig. 5(b), Bi_2Se_3 possesses a significantly higher carrier concentration than the S-rich samples (Bi_2S_3, Bi_2S_2Se, etc.), driven by its narrower band gap (0.43 eV) and the weaker electron-binding ability of Se. Consequently, this high carrier concentration results in a low absolute Seebeck coefficient for Bi_2Se_3. $Bi_2S_{0.5}Se_{2.5}$, exhibiting the highest electrical conductivity (1656.54 S·cm^{-1}), naturally possessed the lowest absolute Seebeck coefficient. The negative S values across the entire Bi–S–Se system confirm n-type conduction behavior. Figure 5(d) shows the PF as a function of temperature. The introduction of Se into the Bi_2S_3 matrix significantly enhanced the power factor. This improvement is primarily ascribed to the substantial increase in electrical conductivity, which effectively compensates for the minor reduction in the Seebeck coefficient.

To elucidate the origin of the enhanced electrical properties, the electronic band structures of $Bi_2S_{3-x}Se_x$ (x = 0, 0.5, 1, 2, 2.5, and 3)

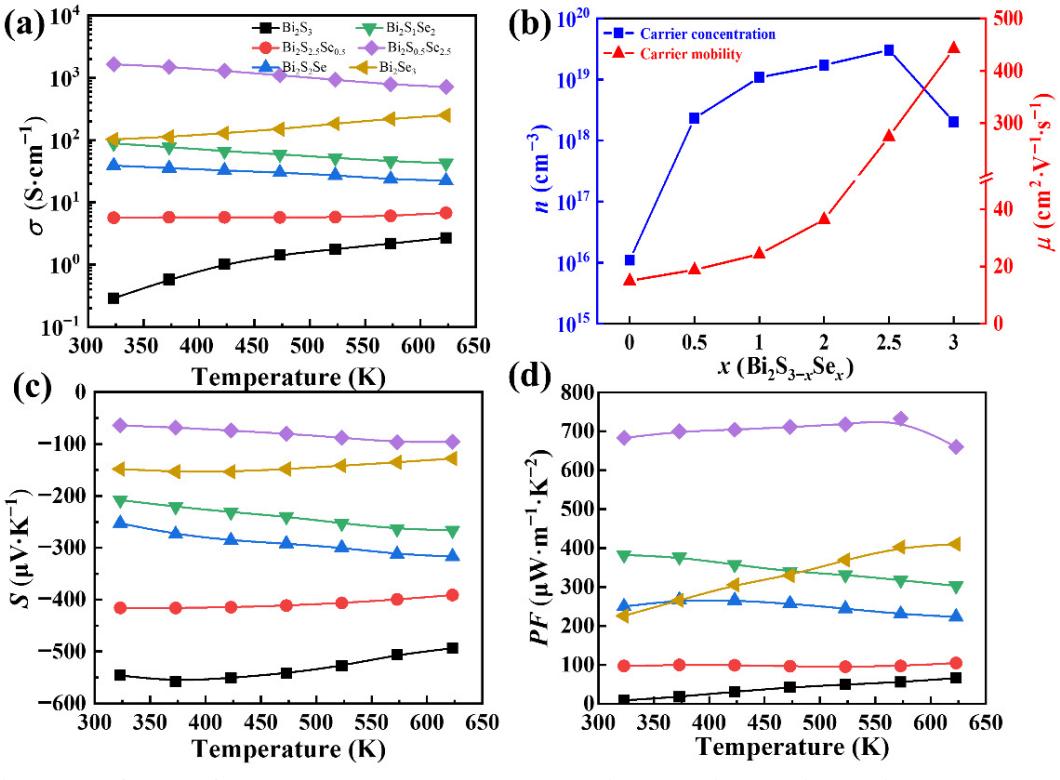

Fig. 5 Electrical transport performance of Bi_2S_3, $Bi_2S_{2.5}Se_{0.5}$, Bi_2S_2Se, Bi_2SSe_2, $Bi_2S_{0.5}Se_{2.5}$, and Bi_2Se_3: (a) electric conductivity; (b) carrier concentration and mobility; (c) Seebeck coefficient; and (d) power factor.

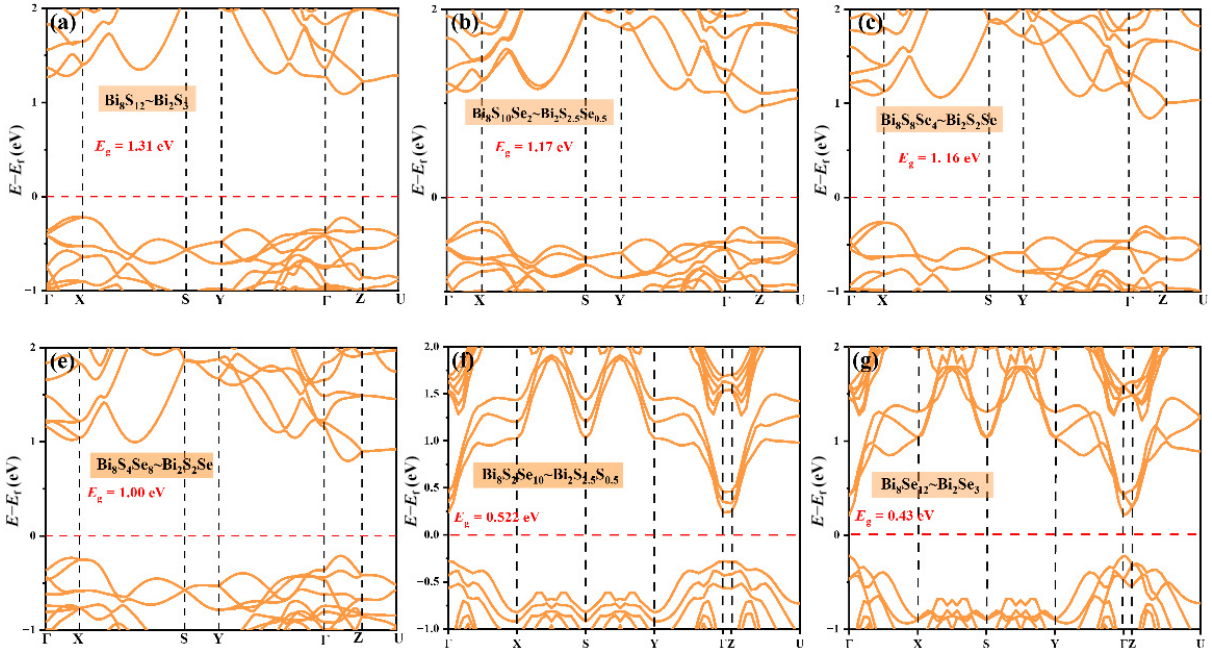

Fig. 6 Band structures of (a) Bi_2S_3, (b) $Bi_2S_{2.5}Se_{0.5}$, (c) Bi_2S_2Se, (d) Bi_2SSe_2, (e) $Bi_2S_{0.5}Se_{2.5}$, and (f) Bi_2Se_3. The left side of the wavy line in the figure represents the experimentally calculated ratio, whereas the right side denotes the nominal ratio.

were calculated using DFT (Fig. 6), revealing a clear trend of progressively narrowing band gaps with increasing Se content. It is evident that as the amount of Se incorporated into Bi_2S_3 increases, the band gap gradually decreases from 1.31 eV for Bi_2S_3 to 0.43 eV for Bi_2Se_3. Although Se replaces the S atoms without introducing additional electrons, its lower electronegativity weakens its electron-binding ability. This reduction facilitates the availability of extra electrons, forming negative centers that cause a downward shift in the conduction band, thereby narrowing the band gap. This weakened electron-binding ability is explicitly supported by the quantitative COHP analysis shown in Fig. 8, which reveals a systematic decrease in bond energy with Se incorporation. Notably, when the Se content reaches a solid solubility of 2.5, the crystal structure changes from the orthorhombic *Pnma* space group of Bi_2S_3 to the rhombohedral $R\bar{3}m$ space group of Bi_2Se_3. This structural transformation from a chain-like to a layered configuration leads to a further reduction in the band gap to 0.49 eV, which remarkably contributes to the enhanced conductivity of $Bi_2S_{0.5}Se_{2.5}$ and Bi_2Se_3, increasing it by an order of magnitude.

The impact of structural evolution on thermal transport is presented in Figs. 7(a)–7(c). The total thermal conductivity of $Bi_2S_{3-x}Se_x$ ($x \leq 2$) is lower than that of Bi_2S_3. While the smaller difference between the ionic radii of Se (198 pm) and S (184 pm) weakens stress field fluctuation scattering, the large mass difference between the relative atomic masses of Se (78.94 pm) and S (32.06 pm) induces stronger mass fluctuation scattering. This leads to an increase in point-defect scattering, which reduces the lattice thermal conductivity of the material. To quantitatively verify this mechanism, the theoretical lattice thermal conductivity was calculated using the Debye–Callaway model. The results, as shown in Table S2 in the ESM, confirm that the mass fluctuation term dominates the phonon scattering process compared to the strain field term. Beyond the point-defect scattering induced by mass fluctuations, the microstructural evolution observed in Fig. 4 also contributes significantly to the reduction in lattice thermal conductivity. The transition from particle-like grains in pristine Bi_2S_3 to lamellar (plate-like) grains in Se-alloyed samples introduces a high density of grain boundaries and planar interfaces. These anisotropic interfaces act as effective scattering centers for phonons, particularly those with medium-to-long mean free paths that are less affected by atomic-scale point defects. Consequently, the synergistic effect of atomic-scale mass fluctuation scattering and microscale interface scattering results in full-frequency phonon scattering, effectively minimizing the lattice thermal conductivity. Bi_2Se_3 shows an upward trend in total thermal conductivity with temperature, which is attributed to the rise in its electronic thermal conductivity. This behavior is linked to its narrower band gap than that of the other compounds, as shown in Fig. 5. The narrow band gap facilitates intrinsic thermal excitation, leading to mixed conduction of electrons and holes. This intrinsic excitation results in a significant bipolar thermal conductivity effect. The recombination of charge carriers releases energy, which, combined with the high electronic thermal conductivity, leads to the observed increase in total thermal conductivity at high temperatures. Figure 7(d) depicts the *ZT* values of $Bi_2S_{3-x}Se_x$ (x = 0, 0.5, 1, 2, 2.5, and 3). Among these, Bi_2SSe_2 exhibits the highest *ZT* value across the entire temperature range (*ZT* = 0.38, 623 K). However, Bi_2SSe_2 does not demonstrate superior electrical or thermal properties compared to the other compositions. This observation highlights a crucial insight for researchers in the field of TE materials: Achieving optimal TE performance does not necessarily require maximizing a single property. Instead, a balanced and synergistic regulation of electrical conductivity, Seebeck coefficient, and thermal conductivity can effectively enhance the overall TE performance.

The density of states (DOS) diagram only reflects the number of electronic states available within each energy range of the material. In contrast, COHP [38] analysis offers a more intuitive assessment of bond strength than the DOS. Therefore, COHP calculations were employed to gain a better understanding of the bonding characteristics of Bi–S–Se. In addition, the integrated COHP (ICOHP) represents the contribution of a chemical bond to the total energy of a particle, reflecting its overall bond strength. Since the energy term is introduced into the COHP calculation, contributions to the negative energy correspond to bonding states,

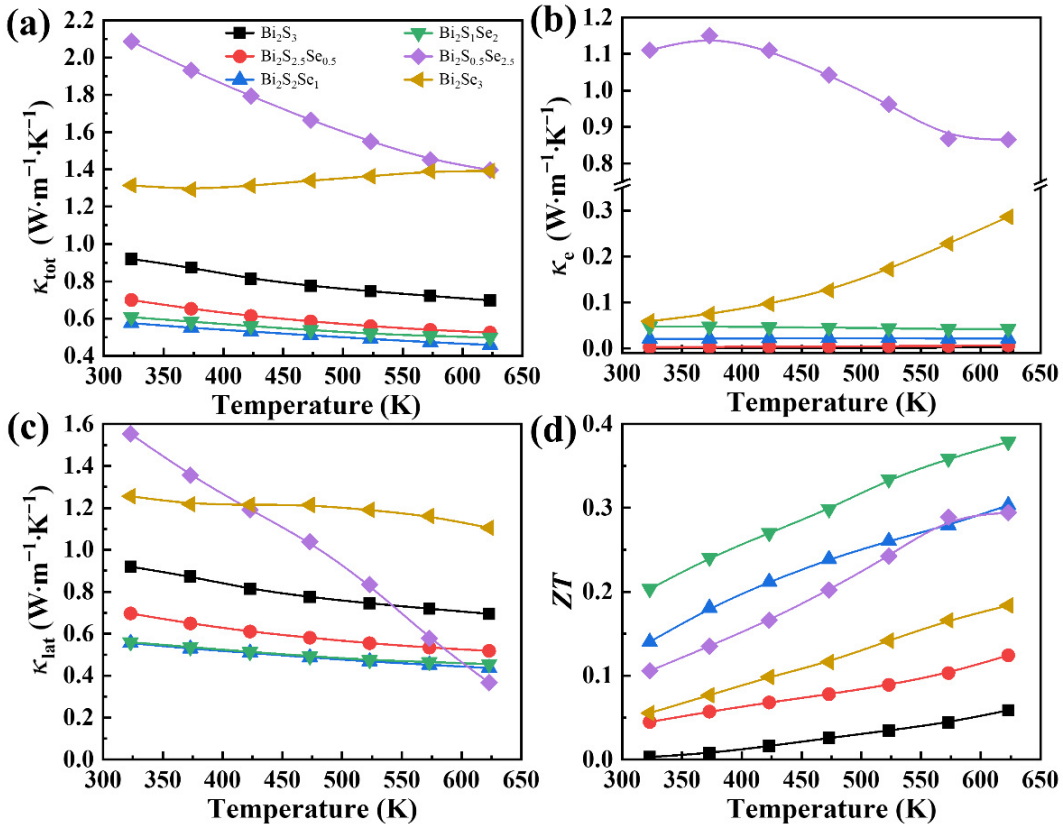

Fig. 7 Thermal performance of Bi_2S_3, $Bi_2S_{2.5}Se_{0.5}$, Bi_2S_2Se, Bi_2SSe_2, $Bi_2S_{0.5}Se_{2.5}$, and Bi_2Se_3: (a) total thermal conductivity; (b) electronic thermal conductivity; (c) lattice thermal conductivity; (d) *ZT*.

whereas contributions to the positive energy indicate antibonding states, denoted as −COHP. The −COHP values for different neighboring atom pairs in Bi–S–Se are shown in Fig. 8. Accordingly, the peaks on the right represent bonding contributions, whereas those on the left suggest antibonding interactions. A larger −COHP value below the Fermi level indicates stronger bonding interactions. As shown in Fig. 8, several chemical bonds exhibit relatively high −COHP values, indicating strong atomic interactions in the following six compounds: Bi_2S_3 (Bi–S1: −COHP = 2.669, Bi–S2: −COHP = 2.484), $Bi_2Se_{0.5}S_{2.5}$ (Bi–S1: −COHP = 2.532, Bi–Se2: −COHP = 2.568), Bi_2SeS_2 (Bi–S1: −COHP = 2.574, Bi–Se2: −COHP = 2.577), Bi_2SSe_2 (Bi–S1: −COHP = 2.503, Bi–Se2: −COHP = 2.501), $Bi_2Se_{2.5}S_{0.5}$ (Bi1–Se1: −COHP = 4.372, Bi2–S2: −COHP = 3.154), and Bi_2Se_3 (Bi–Se1: −COHP = 2.356). With increasing Se solid solubility, the bonding strength of the Bi–S1 bond in Bi_2S_3 gradually weakens. However, the Bi–S1 bond energy in $Bi_2Se_{2.5}S_{0.5}$ is the lowest (−COHP = 1.583), suggesting that it plays a significant role in stabilizing the Bi–S1 bond within the compound.

In addition, the Bi1–Se1 (−COHP = 4.372) and Bi2–S2 (−COHP = 3.154) bonds in $Bi_2Se_{2.5}S_{0.5}$ also make substantial contributions to its structural stability. When the compound transforms into Bi_2Se_3, the Bi1–S1 bond is replaced by the Bi–Se1 bond, which shows stronger bonding than the Bi–S1 bond in $Bi_2Se_{2.5}S_{0.5}$. Notably, the latter exhibits the lowest bond energy among the four compounds studied.

With increasing Se content, the Bi–S2, Bi–S3, and Bi–S4 bonds are progressively transformed into Bi–Se2, Bi–Se3, and Bi–Se4 bonds. In Bi_2S_3, $Bi_2Se_{0.5}S_{2.5}$, Bi_2SeS_2, and Bi_2SSe_2, the bond energies at these sites show minimal variation. However, in $Bi_2Se_{2.5}S_{0.5}$ and Bi_2Se_3, the bond energies at the same positions differ significantly, which is likely attributed to changes in the crystal structure. In contrast, the −COHP values of Bi–S5 vary with Se incorporation, but no clear trend is observed.

It is worth noting that most chemical bonds in $Bi_2Se_{2.5}S_{0.5}$ exhibit higher −COHP values than those in the other materials. A higher −COHP value is typically associated with greater crystal rigidity and faster phonon velocity, which together enhance the lattice thermal conductivity. This inference is supported by thermal performance tests, which show that $Bi_2Se_{2.5}S_{0.5}$ exhibits the highest lattice thermal conductivity among all the compounds studied.

The COHP analysis presented in Fig. 8 further corroborates that the enhancement in carrier mobility arises from a reconstruction of the local electronic environment rather than a transformation in crystallographic symmetry. With increasing Se content, the Bi–Ch (Ch = S or Se) bond strength, as evidenced by the integrated COHP (−ICOHP) values, increases significantly. In particular, the Bi–Se1 and Bi–Se2 bonds exhibit notably higher −ICOHP (4.372 and 2.359 eV, respectively), indicating strong covalency and enhanced orbital overlap. Furthermore, the COHP profiles near the Fermi level become smoother and more delocalized with Se substitution, suggesting reduced carrier localization and scattering. These modifications imply the formation of more coherent and extended electronic transport channels. Therefore, although the global crystal structure remains orthorhombic, the local bonding environment and electronic structure are significantly altered. This local reconstruction effectively redefines the carrier transport pathways within the Bi_2S_3 matrix, explaining the observed monotonic increase in carrier mobility with increasing Se content. Furthermore, the quantitative reduction in bond strength, exemplified by the decrease in the Bi–S1 −ICOHP value from 2.669 in B_2S_3 to 1.583 in the highly

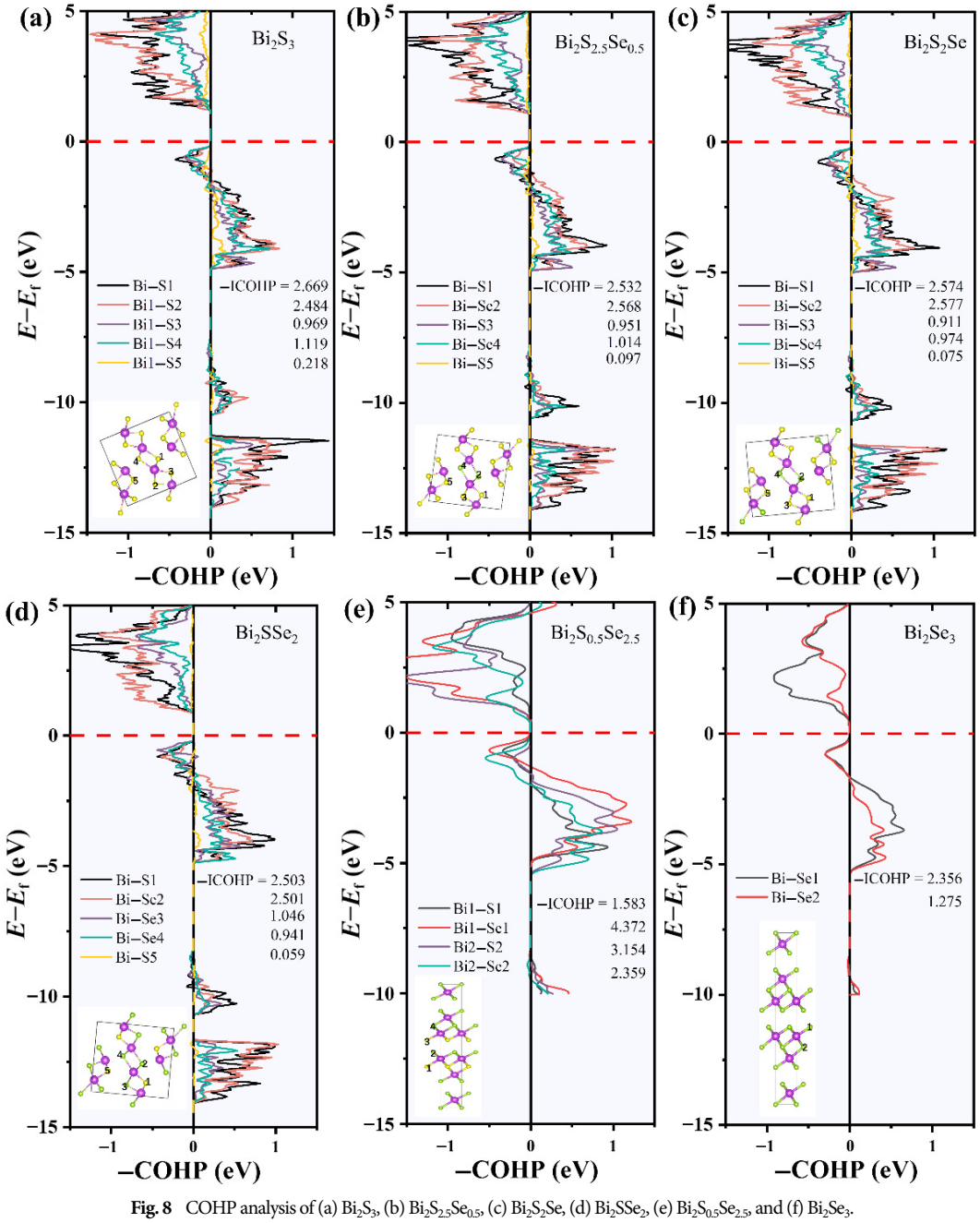

Fig. 8 COHP analysis of (a) Bi_2S_3, (b) $Bi_2S_{2.5}Se_{0.5}$, (c) Bi_2S_2Se, (d) Bi_2SSe_2, (e) $Bi_2S_{0.5}Se_{2.5}$, and (f) Bi_2Se_3.

conductive $Bi_2S_{0.5}Se_{2.5}$, provides the structural origin for the sharp increase in carrier concentration observed in Fig. 5(b).

Beyond the thermoelectric performance, the mechanical reliability of the solid solutions was evaluated. As illustrated in the spatial distribution maps (Figs. 9(a)–9(l)) and the statistical averages (Figs. 9(m) and 9(n)), both Young's modulus and microhardness exhibit a gradual decrease with increasing Se content. The *X* and *Y* coordinates in the diagram correspond to each other. With the incorporation of Se into Bi_2S_3 to form a solid solution, a change in surface color is observed, accompanied by a gradual decrease in Young's modulus and microhardness. The microhardness decreases from 2.5 GPa for pure Bi_2S_3 to a minimum of 1.25 GPa for Bi_2Se_3, representing 50% of the initial value. Similarly, Young's modulus declines from 47.5 GPa for Bi_2S_3 to 37.5 GPa for Bi_2Se_3, which corresponds to 78% of the initial value. This reduction is ascribed to the relatively weakness of Bi–Se bonds compared to the Bi–S bonds. As Se is gradually substituted into the Bi_2S_3 lattice, Bi–S bonds are progressively replaced by Bi–Se bonds. Moreover, a structural phase transition occurs in $Bi_2S_{3-x}Se_x$ ($x \geq 2.5$), as detailed in Figs. 1 and 2. The phase changes from the orthorhombic phase to the prismatic phase and from a chain-like structure to a layered structure. The weak van der Waals forces between the atoms allow these two-dimensional layers to slide relatively easily, which further contributes to the reduction in both Young's modulus and microhardness.

4 Conclusions

In summary, this work demonstrates that incorporating Se into Bi_2S_3 via solid solution effectively modulates the microstructure from granular to lamellar and reconstructs carrier transport channels. This synergistic optimization led to reduced lattice thermal conductivity and enhanced electrical performance, yielding a peak *ZT* of 0.38 at 623 K for the Bi_2SSe_2 sample.

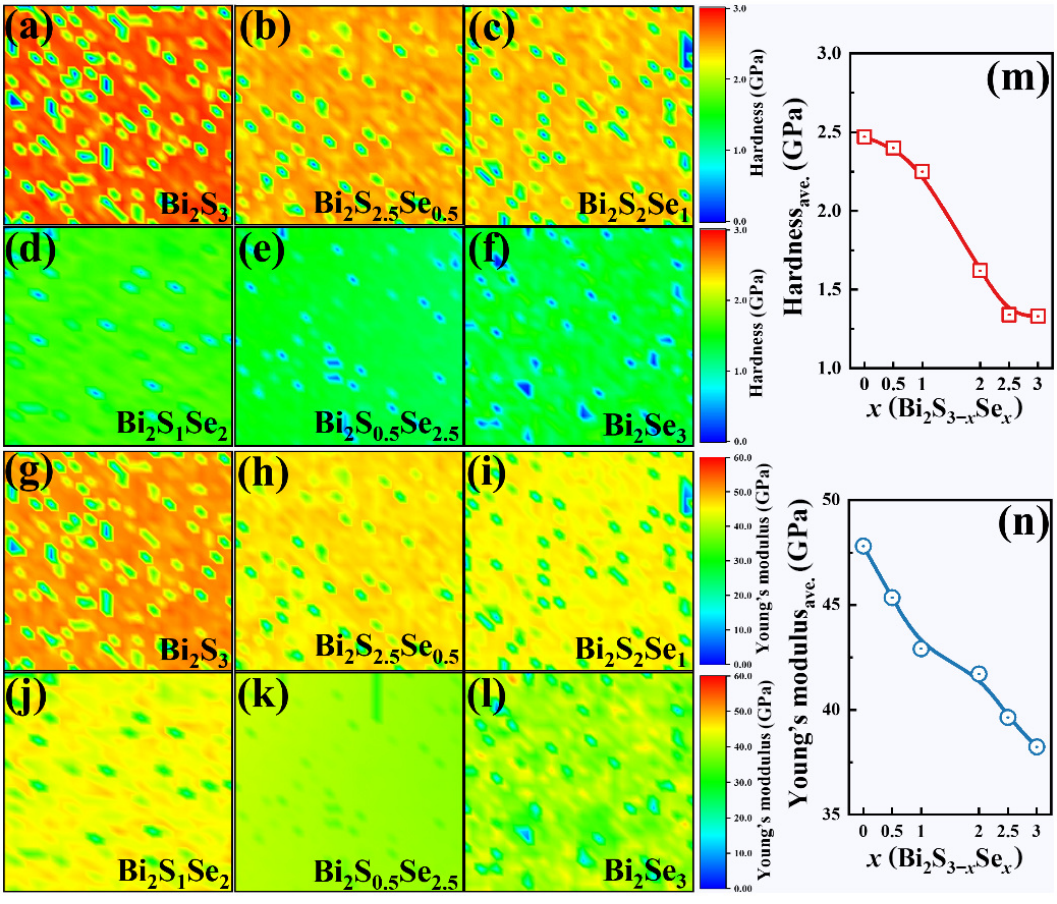

Fig. 9 Microhardness and Young's modulus of all samples with two-dimensional indentation profiles: Bi_2S_3, $Bi_2S_{2.5}Se_{0.5}$, Bi_2S_2Se, Bi_2SSe_2, $Bi_2S_{0.5}Se_{2.5}$, and Bi_2Se_3.

Looking ahead, there is significant potential for further enhancing the performance of Bi–S-based materials. Future research directions should focus on multicomponent codoping strategies (e.g., cation substitution) to decouple electrical and thermal transport parameters. Additionally, nanointerface engineering can be employed to introduce multiscale scattering centers, thereby suppressing lattice thermal conductivity effectively. Finally, beyond transport properties, investigating mechanical reliability and long-term thermal stability will be crucial for integrating these materials into robust mid-temperature power generation modules.

Acknowledgements

We thank the financial support from the National Natural Science Foundation of China (Nos. 52562030 and 12574036), the National Key R&D Program of China (No. 2022YFF0503804), the Academician (Expert) Workstation of Yunnan Province Program (No. 202405AF140066), Yunnan Science and Technology Program (No. 202401AT070403), Yunnan Fundamental Research Projects (No. 202401BE070001-004), and Yunnan Major Scientific and Technological Project (No. 202302AG050010).

Availability of data and materials

The data that support the findings of this study are available from the corresponding author upon reasonable request.

Competing interests

The authors have no competing interests to declare that are relevant to the content of this article. The author Jing Feng is the Editorial Committee member of this journal.

Electronic Supplementary Material

Supplementary material is available in the online version of this article at https://doi.org/10.26599/JAC.2026.9221239.

References

[1] Zhou CJ, Yu Y, Zhang XZ, *et al.* Cu intercalation and Br doping to thermoelectric $SnSe_2$ lead to ultrahigh electron mobility and temperature-independent power factor. *Adv Funct Mater* 2020, **30**: 1908405.

[2] Hsu KF, Loo S, Guo F, *et al.* Cubic $AgPb_mSbTe_{2+m}$: Bulk thermoelectric materials with high figure of merit. *Science* 2004, **303**: 818–821.

[3] Qian X, Guo HR, Lyu JX, *et al.* Enhancing thermoelectric performance of p-type SnTe through manipulating energy band structures and decreasing electronic thermal conductivity. *Rare Metals* 2024, **43**: 3232–3241.

[4] Meroz O, Gelbstein Y. Thermoelectric $Bi_2Te_{3-x}Se_x$ alloys for efficient thermal to electrical energy conversion. *Phys Chem Chem Phys* 2018, **20**: 4092–4099.

[5] Jabar B, Li F, Zheng ZH, *et al.* Homo-composition and hetero-structure nanocomposite *Pnma* Bi_2SeS_2–*Pnnm* Bi_2SeS_2 with high thermoelectric performance. *Nat Commun* 2021, **12**: 7192.

[6] Li JH, Tan Q, Li JF, *et al.* BiSbTe-based nanocomposites with high ZT: The effect of SiC nanodispersion on thermoelectric properties. *Adv Funct Mater* 2013, **23**: 4317–4323.

[7] Sun W, Liu WD, Liu QF, *et al.* Advances in thermoelectric devices for localized cooling. *Chem Eng J* 2022, **450**: 138389.

[8] Kyratsi T, Chung DY, Kanatzidis MG. Bi/Sb distribution and its consequences in solid solution members of the thermoelectric materials $K_2Bi_{8-x}Sb_xSe_{13}$. *J Alloy Compd* 2002, **338**: 36–42.

[9] Du BS, Lai XF, Liu QL, *et al.* Spark plasma sintered bulk

nanocomposites of $Bi_2Te_{2.7}Se_{0.3}$ nanoplates incorporated Ni nanoparticles with enhanced thermoelectric performance. *ACS Appl Mater Inter* 2019, **11**: 31816–31823.
[10] Hu YX, Bai SL, Qin BC, *et al.* Magnetics for thermoelectric enhancement. *Electromag Sci* 2025, **3**: 0100611.
[11] Bai SL, Qin BC, Zhao LD. Role of carrier mobility in decoupling electron–phonon transport contradiction. *J Chin Ceram Soc* 2025, **53**: 733–741. (in Chinese)
[12] Zhou JY, Chen ZW, Luo J, *et al.* Gradient doping enables an extraordinary efficiency in thermoelectric $PbTe_{1-x}I_x$. *Adv Mater* 2024, **36**: 2405299.
[13] Sherchenkov A, Borgardt N, Shtern M, *et al.* The role of nanostructuring strategies in PbTe on enhancing thermoelectric efficiency. *Mater Today Energy* 2023, **37**: 101416.
[14] Huang M, Zhai PC, Li GD, *et al.* Nanotwin-induced ductile mechanism in thermoelectric semiconductor PbTe. *Matter* 2022, **5**: 1839–1852.
[15] Sun JC, Zhang Y, Fan YT, *et al.* Strategies for boosting thermoelectric performance of PbSe: A review. *Chem Eng J* 2022, **431**: 133699.
[16] Deng Q, Zhang FJ, Nan PF, *et al.* Unique semi-coherent nanostructure advancing thermoelectrics of N-type PbSe. *Adv Funct Mater* 2024, **34**: 2310073.
[17] Liu SB, Qin BC, Zhao LD. PbSe thermoelectrics: Efficient candidates for power generation and cooling. *Adv Energy Mater* 2025, **15**: 2404251.
[18] Huang YL, Zhang B, Li JW, *et al.* Unconventional doping effect leads to ultrahigh average thermoelectric power factor in Cu_3SbSe_4-based composites. *Adv Mater* 2022, **34**: 2109952.
[19] Wei TR, Wang H, Gibbs ZM, *et al.* Thermoelectric properties of Sn-doped p-type Cu_3SbSe_4: A compound with large effective mass and small band gap. *J Mater Chem A* 2014, **2**: 13527–13533.
[20] Meng F, Sun S, Ma J, *et al.* Anisotropic thermoelectric figure-of-merit in Mg_3Sb_2. *Mater Today Phys* 2020, **13**: 100217.
[21] Li JK, Chetty R, Liu ZH, *et al.* Enhancing the thermoelectric performance of n-type Mg_3Sb_2-based materials via Ag doping. *Small* 2025, **21**: 2408059.
[22] Shi XM, Wang X, Li W, *et al.* Advances in thermoelectric Mg_3Sb_2 and its derivatives. *Small Methods* 2018, **2**: 1800022.
[23] Chen ZW, Jian ZZ, Li W, *et al.* Lattice dislocations enhancing thermoelectric PbTe in addition to band convergence. *Adv Mater* 2017, **29**: 1606768.
[24] Wang L, Wen Y, Bai SL, *et al.* Realizing thermoelectric cooling and power generation in N-type $PbS_{0.6}Se_{0.4}$ via lattice plainification and interstitial doping. *Nat Commun* 2024, **15**: 3782.
[25] Yu Y, Sheskin A, Wang ZY, *et al.* Ostwald ripening of Ag_2Te precipitates in thermoelectric PbTe: Effects of crystallography, dislocations, and interatomic bonding. *Adv Energy Mater* 2024, **14**: 2304442.
[26] Chen XX, Wu HJ, Cui J, *et al.* Extraordinary thermoelectric performance in n-type manganese doped Mg_3Sb_2 Zintl: High band degeneracy, tuned carrier scattering mechanism and hierarchical microstructure. *Nano Energy* 2018, **52**: 246–255.
[27] Banik A, Shenoy US, Anand S, *et al.* Mg alloying in SnTe facilitates valence band convergence and optimizes thermoelectric properties. *Chem Mater* 2015, **27**: 581–587.
[28] Wang DY, Ding JM, Ma YQ, *et al.* Multi-heterojunctioned plastics with high thermoelectric figure of merit. *Nature* 2024, **632**: 528–535.
[29] Yang TY, Gu SW, Zhang YX, *et al.* Pseudopolymorphic phase engineering for improved thermoelectric performance in copper sulfides. *Adv Mater* 2024, **36**: 2308353.
[30] Balijapelly S, Hauble A, Sundaramoorthy S, *et al.* Ultralow lattice thermal conductivity in the aikinite structure family, $Cu_xPb_xBi_{2-x}S_3$, and thermoelectric properties of $Cu_{0.14}Pb_{0.14}Bi_{1.86}S_3$. *ACS Appl Energy Mater* 2022, **5**: 14222–14230.
[31] Liufu SC, Chen LD, Yao Q, *et al.* Assembly of one-dimensional nanorods into Bi_2S_3 films with enhanced thermoelectric transport properties. *Appl Phys Lett* 2007, **90**: 112106.
[32] Guo J, Ge ZH, Qian F, *et al.* Achieving high thermoelectric properties of Bi_2S_3 via $InCl_3$ doping. *J Mater Sci* 2020, **55**: 263–273.
[33] Yang J, Yan JN, Liu GW, *et al.* Improved thermoelectric properties of n-type Bi_2S_3 via grain boundaries and *in-situ* nanoprecipitates. *J Eur Ceram Soc* 2019, **39**: 1214–1221.
[34] Guo J, Yang JM, Ge ZH, *et al.* Realizing high thermoelectric performance in earth-abundant Bi_2S_3 bulk materials via halogen acid modulation. *Adv Funct Mater* 2021, **31**: 2102838.
[35] Zhang L, Liu H, Shen YZ, *et al.* Boosting the thermoelectric performance of Bi_2S_3 by $CeCl_3$ addition and hydrothermal synthesis. *Ceram Int* 2024, **50**: 50982–50988.
[36] Zhu Y, Wang XY, Shen YL, *et al.* High thermoelectric performance in n-type bismuth sulfide by carrier concentration tuning and dense nanodomains. *J Eur Ceram Soc* 2024, **44**: 5096–5104.
[37] Zou J, Wang DZ, Bi Z, *et al.* Enhancement of thermoelectric performance in Bi_2S_3 enabled by pressure-induced electronic topological transition. *Appl Phys Lett* 2025, **127**: 103902.
[38] Dronskowski R, Bloechl PE. Crystal orbital Hamilton populations (COHP): Energy-resolved visualization of chemical bonding in solids based on density-functional calculations. *J Phys Chem* 1993, **97**: 8617–8624.